Materials & Design 265 (2026) 115887

Contents lists available at ScienceDirect

Materials & Design

journal homepage: www.elsevier.com/locate/matdes

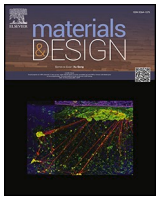

From Earth's Crust to Composite Design: A Numerical and Experimental Study of Lithosphere-Inspired Polymeric Multi-Layer Composites

Christoph Waly [a,b], Martin Pletz [c,*], Tim Volders [d], Marco Contino [e], Federico Passoni [e], Davide Ruffoni [d], Luca Andena [e], Florian Arbeiter [a,b]

[a] Institute of Materials Science and Testing of Polymers, Technical University of Leoben, Otto Gloeckel-Strasse 2, 8700 Leoben, Austria
[b] Christian Doppler Laboratory for Impact of recycled materials on the mechanical lifetime estimation of polymers, Institute of Materials Science and Testing of Polymers, Technical University of Leoben, Austria
[c] Institute of Designing Plastics and Composite Materials, Technical University of Leoben, Otto Gloeckel-Strasse 2, 8700 Leoben, Austria
[d] Mechanics of Biological and Bioinspired Materials Laboratory, Department of Aerospace and Mechanical Engineering, University of Liège, Quartier Polytech 1, 4000 Liège, Belgium
[e] Dipartimento di Chimica, Materiali e Ingegneria Chimica "Giulio Natta", Politecnico Di Milano, 20133 Milan, Italy

ARTICLE INFO

Keywords:
Lithomimetics
Lithomer
TangoBlack
Verowhite
Multi-material additive manufacturing
Fracture testing

ABSTRACT

Compliant flat interlayers (IL) embedded into a cracked stiff matrix improve damage tolerance in polymeric systems, but typically at the cost of reduced stiffness and lower crack-initiation forces. To mitigate these limitations, a design approach originating from the Earth's lithosphere was adopted. In particular, a symmetric wavy compliant IL was embedded into a stiff matrix, and a numerical model was established in ABAQUS to identify promising geometries via a systematic variation of wave height, wavelength, and the relative position of the wave to the initial crack. Numerical results demonstrate that stiffness, crack-initiation force, and total energy dissipation strongly vary with IL geometry. Compared to the flat IL, wavy ILs continuously enhance stiffness and crack-initiation force, albeit with reduced energy absorption. The crack position relative to the wavy IL shows only minor influence on the global fracture response. Based on the numerical results, seven variants were selected and fabricated using PolyJet technology and experimentally examined. The experimental results confirm the numerical predictions, demonstrating good agreement in the initial force–displacement regime, which validates the numerical model as an efficient tool for preliminary design screening. Beyond crack initiation, linear-elastic assumptions lead to deviations, limiting the models applicability to the early fracture stage.

1. Introduction

Continuously increasing demands on load-bearing structural applications, such as in transportation, construction, or even sports goods, often require the full exploitation of material potential up to its physical limits. In this respect, two key material properties often stand in opposition. On one hand, high stiffness and strength to sustain large loads, and on the other, high fracture toughness to prevent sudden, catastrophic failure. Simultaneously achieving both requirements remains a major challenge for conventional engineering materials [1], as enhancements in one property often come at the expense of the other.

To overcome this conflict, materials scientists are increasingly turning to design principles found in both animate and inanimate matter. Particular attention has been given in the past to hierarchically structured materials from living nature, where stiff and compliant phases are combined in a rich variety of motifs. Such architectures can be found, for example, in the microstructure of the deep-sea sponges' skeleton [2–4], where sequential embedding of compliant interlayers (IL) within a stiff matrix leads to significant improvements in fracture toughness, often by several orders of magnitude compared to the pure (brittle) matrix material [5–12]. This enhancement is primarily attributed to the spatial variation in mechanical properties (i.e., Young's modulus and/or yield strength), which locally modulates the crack-driving force (CDF). This effect is commonly referred to as the material inhomogeneity effect [6–8].

Despite this potential, these concepts also face limitations, especially when assuming bending as the prevalent loading mode. The incorporation of compliant ILs inevitably reduces the overall stiffness of the

* Corresponding author.
E-mail address: martin.pletz@unileoben.ac.at (M. Pletz).

https://doi.org/10.1016/j.matdes.2026.115887
Received 9 January 2026; Received in revised form 5 March 2026; Accepted 19 March 2026
Available online 22 March 2026

structure. Although the design offers considerable flexibility regarding the positioning [9], number [9,10,13], and thickness [12] of compliant layers, a trade-off between fracture toughness and the resulting strength and stiffness must still be expected. Particularly in cases of strong mechanical contrast between matrix and compliant IL, stress transfer may become fully decoupled, as stresses cannot be effectively transmitted across the compliant IL [9]. In such cases, the matrix ligaments behave as isolated beams, resulting in a significant loss of stiffness, often deemed unacceptable depending on the specific application.

Naturally, there exist numerous strategies to address the described drawback of stiffness reduction. Inspirations can come, for example, from the rich toolbox of living nature (e.g., nacre) [11,14–16], from the creative thinking of scientists (e.g., heterostructure and lattice materials) [15,17–20], or be derived from simulation-driven design studies [21–23]. However, a major challenge still remains. How to transfer these, often quite complex designs, into large-scale industrial production using polymers. Conventional manufacturing processes, such as extrusion, may struggle to reproduce highly intricate structures, limiting their practical applicability in structural components. Amidst these challenges, certain concepts show particular potential for overcoming the stiffness-toughness trade-off. One of these concepts is the lithomimetic design principle, first introduced by Beygelzimmer et al. [24] in 2021. This concept draws its primary inspiration from structures and patterns naturally occurring within the Earth's lithosphere. Even though such structures can be as complex as those in biological systems, they differ fundamentally in origin and function. While biological materials are evolutionarily tuned for specific tasks, typically hierarchically organized and even show adaptive ability [3,25], lithomimetic structures emerge primarily through physicochemical self-organization, often as a result of plastic deformation under extreme pressure and temperature conditions [24], without the benefit of a natural selection process. Their translation into materials science thus serves more as a design inspiration than as a function-specific blueprint. In other words, structures found in minerals or the Earth's lithosphere do not necessarily enhance specific properties for a given application, but rather offer guiding motifs for material design [15,24,26].

Against this background, the idea of embedding undulating (wave-like) compliant ILs instead of flat ones into a stiff matrix offers distinct advantages. As demonstrated, for example, by Waly et al. [27], such geometries enrich the complexity of the stress state within the compliant IL by coupling not only shear stresses but also tensile and compressive ones. This change leads to a more efficient load transfer in bending and an increased overall stiffness. Moreover, depending on the specific architecture of the compliant IL, geometrical interlocking may be induced, thereby further reducing stress-transfer decoupling and mitigating stiffness degradation. This concept has been shown to improve performance not only in polymeric multi-layer systems but also in metallic [28,29] or ceramic/polymeric systems [30].

A central challenge, however, is the vast number of possible design parameters, such as layer thickness, amplitude, wavelength, radius of curvature, etc., to be defined in a lithospheric structure. Effective material optimization, therefore, requires guidance by a numerical approach that can predict both the structure's stiffness and failure behavior.

The toughening behavior of layered architectures has been vastly investigated through numerical modeling approaches [6,8,31,32], including also the debonding of material interfaces [33]. Toughening effects, arising from the interaction of multiple materials, can be numerically predicted either by analyzing the variation of the CDF during crack growth [6] or by applying crack initiation criteria to both the matrix alone and together with the interface [34]. Commonly used initiation criteria, such as those proposed by Leguillon [35] or Taylor [36], can also be integrated into FEM simulations involving non-planar ILs.

However, predicting crack propagation in structures containing non-planar interfaces is considerably more complex. The crack path may deviate from a straight line, requiring not only the evaluation of the CDF as a function of crack length but also the prediction of the evolving crack trajectory. Such modeling can be achieved using incremental crack-growth approaches in FEM, relying on the J-integral vector or configurational forces to determine propagation direction [37–39], or through more advanced techniques such as XFEM or phase-field methods [40]; the latter approach additionally allows prediction of crack initiation [41]. The stiffness of the bending beam can be directly computed in FEM simulations, including the crack propagation stage.

Based on the problem outlined above, this study aims to explore the potential of wavy ILs in increasing the stiffness of beams loaded in bending compared to flat ILs, while keeping the benefit of increased fracture energy. To this end, a numerical model with linear-elastic material behavior is developed to describe the initial stiffness and the first force drop associated with the propagation of the initial crack into the IL. Using experimentally determined material parameters from an additively manufactured system consisting of "stiff" and "compliant" phases, a parametric study is conducted to quantify the influence of key geometric parameters, such as wavelength, amplitude, and the relative alignment of the wave with respect to the initial crack. Based on this analysis, a wave configuration is identified that maximizes bending stiffness while ensuring sufficient fracture energy.

Using this optimized design as a reference, a design of experiment (DOE)-like set of seven variants (each involving a systematic variation of one key parameter) is manufactured and tested according to existing fracture mechanical standards. For the initial portion of the force–displacement curves, $F(u)$, where plasticity of the matrix material is of minor relevance, the elastic model is validated with the experimental results.

2. Numerical and experimental methodology

Within this study, the numerical and experimental investigations focus on a composite sample with a soft IL embedded within a single-edge notched bending (SENB) specimen subjected to three-point

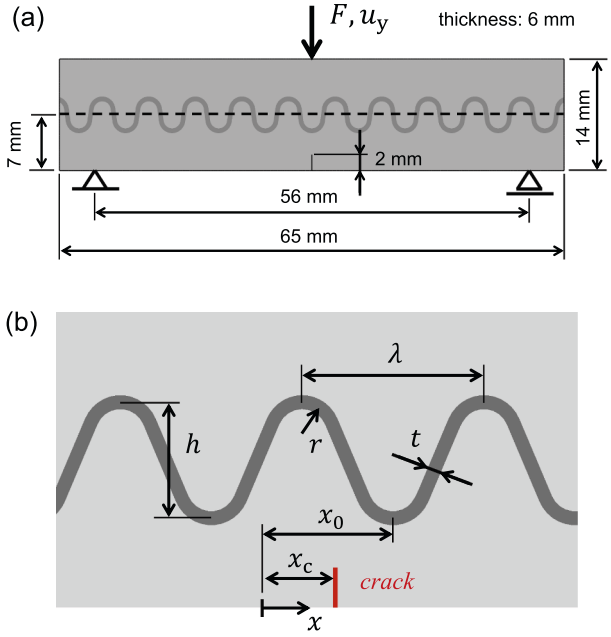

Fig. 1. The dimensions and load application of the specimens used for numerical and fracture mechanics analysis with an IL at half the specimen's thickness (a). Definition of the geometric parameters of the IL and initial crack: height h, wave radius r, wavelength λ, IL thickness t, horizontal shift x_0 of the IL, and initial crack position x_c (b). The origin of the coordinate x is defined at the center of the specimen.

bending, as schematically illustrated in Fig. 1.

The presented wave features a repeating, symmetric fold design, which was selected over alternative, more complex configurations (e.g., recumbent wave designs, as shown, e.g., in Ref. [42]) for two main reasons. First, this geometry represents the most straightforward abstraction of geological folding that can be transferred into laboratory-scale test specimens. Owing to its geometric simplicity and translational symmetry, the design also offers a feasible pathway for implementation in application-relevant components, such as plates or pipes, using continuous manufacturing processes, including extrusion. More complex fold geometries would significantly increase manufacturing complexity and may limit scalability. Second, a previous study [27] has demonstrated that this simplified wave geometry is sufficient to induce a pronounced increase in structural stiffness, due to increasing stress complexity within the compliant IL, while preserving a substantial level of energy absorption. This indicates that the essential mechanical benefits of folded ILs can be captured without resorting to more elaborate geometrical features, thereby justifying the use of the design in the present work.

The specimen dimensions shown in Fig. 1a were chosen to be 65 × 14 × 6 mm^3, based on preliminary testing on the individual materials. The initial crack length, a_0, was kept constant at 2 mm, resulting in an a_0/W ratio of approx. 0.14, and was selected to maintain a broad design space. Specifically, this ratio was chosen to avoid placing the initial crack too close to the compliant IL, which could otherwise lead to increased plastic deformation prior to crack initiation and dynamic effects at crack onset. At the same time, it prevents edge effects on the load-introduction side during advanced crack propagation. Further details regarding the design space are provided in Section 2.2. In any case, it should be noted that the selected ratio does not comply with the recommendations of several fracture mechanics standards, such as ASTM D5045 [43] or ISO 13586 [44], which are not applicable in the present case anyway due to the presence of a compliant IL.

The compliant, curved IL, shown in light gray in Fig. 1a, was positioned symmetrically about the specimen midline and subsequently varied in the numerical study. Fig. 1b provides a detailed view of the curved compliant IL along with all geometric parameters of interest. These parameters essentially include the IL thickness, t; the wave height, h; the wavelength, λ; and the radius, r, of the wave peaks and troughs. In addition to these geometric parameters, the position of the initial crack, x_c, relative to a wave peak or trough could also play a significant role, which must be considered, as the fracture behavior may be affected by a horizontal shift of the wave, x_0.

2.1. Materials & model setup

For simulating crack propagation in the SENB specimens, two finite element models were employed: a) a full 2D model capable of capturing arbitrary crack paths, and b) a symmetric 2D model restricted to describe only straight crack propagation. First, the full 2D model was used to investigate the influence of x_c on both the crack path and the force–displacement, $F(u)$, curve. Then, the symmetric model, which computed much faster, was utilized for the parametric study involving a large number of design variations.

Both models were implemented in ABAQUS 2020 (Dassault Systèmes, France) and were meshed using linear plane stress elements with reduced integration (CPS4R). The non-linear geometry option was selected. The material behavior implemented in the numerical models was based on experimental characterization. VeroWhitePlus (VW+) was used as the stiff matrix material, while the compliant TangoBlackPlus (TB+) represented the IL material. Both polymeric inks were fabricated into single-dumbbell tensile specimens using an inkjet 3D printing process before mechanical testing. Details of the specimen fabrication and tensile test procedure are provided in the supporting information. Both the matrix and the IL material were modeled linear-elastically with the properties obtained from the tensile tests: $E = 2029$ MPa, $\nu = 0.42$ and $E = 6.8$ MPa, $\nu = 0.48$, respectively. In all models, a perfect cohesion between matrix and IL was assumed. The value of the critical stress intensity factor, K_{Ic}, of VW+ was calibrated using the symmetric 2D model without an IL, based on an average a_0 of 2.197 mm and a first peak load, F_c^0, of 104.5 N from the experiments as 0.59 MPa $\sqrt{m}$ (with the energy release rate $G = K^2/E$ for plane stress). The critical stress for crack initiation from the IL (once the initial crack has propagated into it) was set to 125 MPa to enable a qualitative comparison of the total absorbed energy, E_{tot}, across different designs. However, due to the pronounced plastic deformation observed once the crack propagated into the compliant IL of the designs, predicted E_{tot} values were not quantitatively compared to the experiments. For assessing the initial stiffness, S_0, and the first drop in force, F_c^0, however, the non-linearity of both matrix material and IL material can be neglected.

The setup and the results of the full 2D model are presented in the supporting information, whereas the symmetric 2D model is defined in the following.

2.1.1. Symmetric 2D model and definition of model output

A symmetric 2D model shown in Fig. 2 is set up where the crack can only propagate in the symmetry plane. Therefore, the model does not need to check for the crack propagation direction but only open nodes (deactivate their u_x boundary condition) in the symmetry plane to model the crack extension (as described in Ref. [34]). The limitation of x-symmetry allows only a displacement of the IL wave by 0 or $\lambda/2$. The model is much faster to compute and is therefore used for the parametric study of h, r and λ.

Regarding the stiffness, to better fit experiments, the load is applied via rigid supports; contact to the specimen surfaces is modeled using a penalty algorithm, both for normal and tangential contact, with a friction coefficient of $\mu = 0.2$. To avoid the contact stiffness influencing the beam stiffness, a larger $u_{load} = 0.2$ mm is applied in this symmetric model compared to the full model. The bottom support (radius $r = 5$ mm) is completely fixed and the upper fin (also $r = 5$ mm) is moved vertically by u_y but with $u_x = \varphi_z = 0$. The mesh size in the model is set to 0.2 mm.

For $x_0 = 0$, the crack propagates into the wave trough and then reinitiates at an upper wave crest. This means that there is a gap between the position of a crack running into it and then where a crack initiates from the IL. For the stiffness of the specimen, it makes a significant difference if the IL in this gap opens (by failing itself or by debonding of the IL-matrix interface) or not. Therefore, an additional step is added to the symmetrical model: once the crack has reached the IL, the IL's stiffness between this point at $x = 0$ and the next upper wave crest is reduced to a very small stiffness $E = 0.0001$ MPa. Before and after this step, the stiffness and the maximum stress are evaluated. With these two

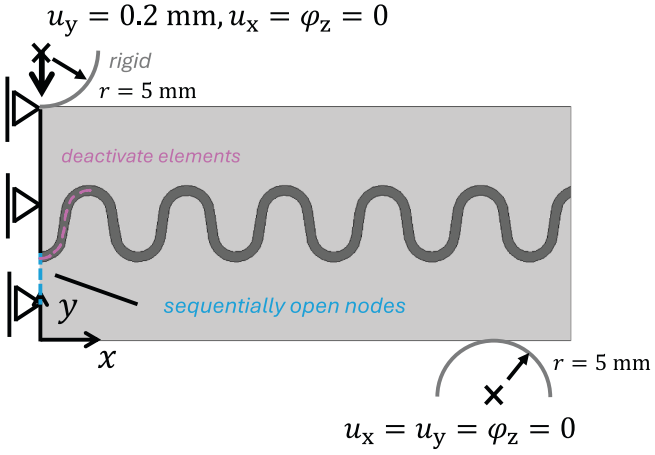

Fig. 2. Setup of the symmetrical model used in the parametric study.

results, two separate $F(u)$ curves can be evaluated, with or without considering debonding.

To define the key output of the model, Fig. 3 shows a typical $F(u)$ curve of the bending beam. The force linearly increases in the beginning with an initial stiffness, S_0, up to the force F_c^0, where the initial crack starts to initiate and propagate. In the displacement-controlled model, this means that the force drops at that displacement. Once the crack has propagated into the IL, the crack is stopped. From that point, F and u increase again with the reduced stiffness of the beam, S_1, due to the propagated crack. Once a criterion for crack initiation from the IL is fulfilled at F_c^1, a crack re-initiates, and the force drops to zero, assuming unstable crack propagation at that point.

For the design in Fig. 3, a crack would initiate from an upper peak of the wavy IL, with a horizontal gap between the initial crack propagated into the IL and the position of crack initiation. Therefore, failure of the IL or a debonding of the matrix-IL interface in this region can affect the shape of the $F(u)$ curve. As an extreme case, a full debonding of the interface can be modelled, which is shown in Fig. 3 by the dashed curve that has an additional drop in force after the F_c^0 and has lower values of S_1 and F_c^1. In reality, debonding may occur gradually upon increasing the load after the first crack propagation, so the two curves give the extremes of the $F(u)$ curves.

To use the beam in a bending setup, a high S_0 and a high F_c^0 are required. However, if the load is too high, it is preferable not to have an abrupt failure when F_c^0 is reached, but to have a higher E_{tot}. As shown in Fig. 4, a beam with bulk matrix material (full) has a large $S_0 = 589.1$ N/mm and $F_c^0 = 104.7$ N, but then fails at rather low applied displacement and therefore low E_{tot} values. With a flat IL, E_{tot} is much higher, but $S_0 = 246.3$ N/mm and $F_c^0 = 70.1$ N considerably drop compared to the bulk material. This can be partially overcome by using a wavy IL (waves), with the design shown in Fig. 4 increasing S_0 to 436.2 N/mm and F_c^0 to 80.9 N but with a lower E_{tot} than the flat design.

Compared to the flat IL with only the IL thickness as a parameter, the wavy IL has many more parameters, such as the overall height, wave shape, and wavelength [27].

2.1.2. Parametric study to identify sample geometries

The full parametric study was conducted using the efficient symmetrical 2D model described in Section 2.1.1, which is applicable for the two symmetry cases, $x_0 = 0$ and $x_0 = \lambda/2$, where the geometry is completely symmetric. From the wave parameters defined in Fig. 1b, a range of practically relevant values was selected, guided by both manufacturing constraints and the findings of the preliminary studies presented above.

The parameter values considered are summarized in Table 1, resulting in a total of 120 parameter combinations. For the cases with $x_0 = 0$, the corresponding $F(u)$ curves were evaluated both with and without debonding.

The selection of the parameters, both in terms of their ranges and the number of values considered, is motivated as follows:

- Wavelength λ: λ is selected within a range comparable to the specimen dimensions to allow for clear observation of possible crack deviations. Moreover, λ must remain significantly larger than t. Very large λ are not expected to produce substantial increases in S_0. Thus, values of λ between 6 mm and 12 mm are investigated.
- Wave height h: h must be sufficiently small to ensure that a_0 of 2 mm does not extend into the compliant IL. With the wave positioned at half the specimen height, a maximum of 10 mm is available. Subtracting t of 0.6 mm leaves 9.4 mm of free space. Accordingly, $h \leq 8$ mm is chosen to prevent the initial crack tip from approaching the IL too closely.
- Wave radius r: Considering that at F_c^1, a crack initiates from the wave peak, a larger r is generally advantageous. A sharp corner ($r = 0$) is excluded due to the stress singularity in the stress-based crack initiation model. Moreover, the maximum permissible r is constrained by the λ definition, such that $r \leq \lambda/4$. Considering the smallest λ investigated ($\lambda = 6$ mm), r is varied between 0.4 mm and 1.4 mm in three increments. Importantly, the upper bound of r is not increased for larger r to maintain consistency across different values of λ.
- IL thickness t: To minimize reduction of the overall stiffness while still enabling effective crack arrest, t should be as small as possible. The minimum feasible t is determined by the printing resolution and the formation of an interphase layer [45]. Prior experiments confirmed that a uniform IL can be reliably achieved with $t = 0.6$ mm, which is therefore chosen for all designs.
- Wave offset x_0: As shown previously, the two cases $x_0 = 0$ and $x_0 = \lambda/2$, both with the initial crack located at the specimen center ($x_c =$

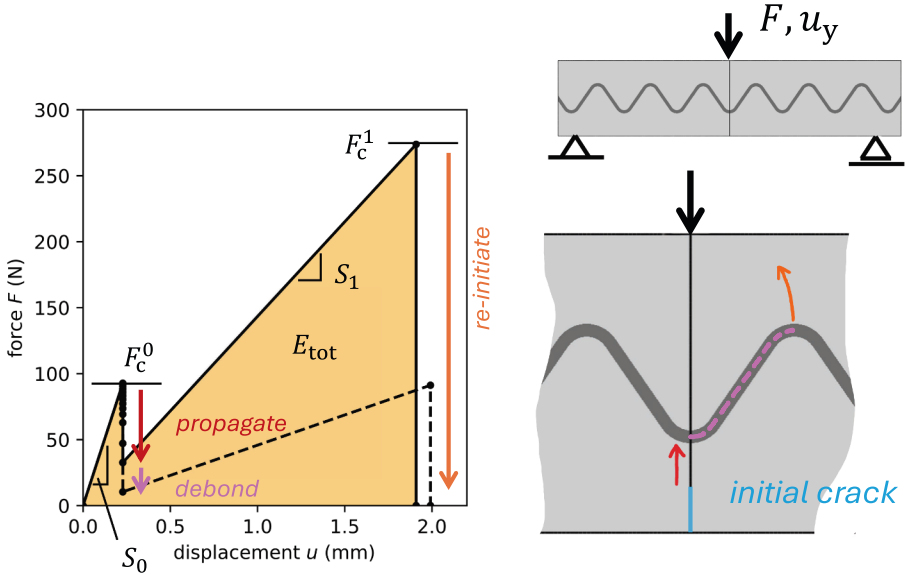

Fig. 3. General output of the bending model seen in the $F(u)$ curve: S_0, F_c^0, F_c^1, and E_{tot}. Once the crack has propagated into the IL, there are two options simulated in the symmetric 2D model: a) the IL and the IL/matrix interfaces can stay intact (solid $F(u)$ curve) or b) the IL can debond until the next peak of the IL wave, indicated in magenta and by the dashed $F(u)$ curve. (For interpretation of the references to colour in this figure legend, the reader is referred to the web version of this article.)

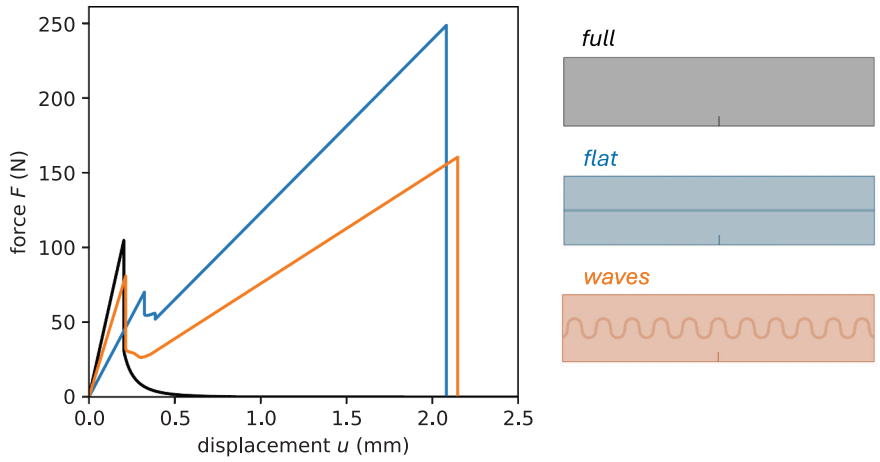

Fig. 4. $F(u)$ curves for three bending specimens computed with the symmetric model: a) bulk (full) matrix material, b) a flat IL, and c) a wavy IL. First crack propagation occurs at lower applied forces in the beams with ILs, but the force for ultimate failure is much larger than in the full material (particularly for the flat IL). Note that the beam with the wavy IL has a larger initial stiffness than the beam with a flat IL.

Table 1
Range of wave parameters used in the parametric study.

Parameter	Value
wavelength λ (mm)	6, 8, 10, 12
wave height h (mm)	0, 2, 4, 6, 8
wave radius r (mm)	0.4, 0.9, 1.4
IL thickness t (mm)	0.6
wave offset x_0 (mm)	0,λ/2
crack position x_c (mm)	0

0), represent the two limiting scenarios for relative crack position. Accordingly, only these two cases are included in the parametric study.

- Crack position x_c: The previous studies demonstrated that the crack path is primarily governed by the relative position of the initial crack and the wave ($x_0 - x_c$). Consequently, x_c is fixed at 0, and only x_0 is varied.

2.1.3. *Selected wave designs for fracture testing*

In addition to the matrix material without an IL (further referred to as design full) and the specimen with a flat IL (design flat), both serving as reference configurations, a wavy IL design was selected based on the results of the parametric study presented in Section 3.1. This design, hereafter referred to as design 0, corresponds to the configuration associated with the highest initial stiffness, S_0. It is characterized by a λ of 6 mm, a h of 4 mm, and a horizontal wave position of $x_0 = 0$. r was chosen as large as possible for $\lambda = 6$ mm, resulting in $r = 1.4$ mm.

Building upon design 0, the parameters h, λ, and x_0 are separately changed to identify their influence on the $F(u)$ curves, while keeping all the other parameters of design 0. h is reduced and increased to 2 mm and 6 mm, respectively. λ is only increased up to 10 mm, and the relative wave position is additionally set to $\lambda/4 = 1.5$ mm and $\lambda/2 = 3$ mm. t, as mentioned previously, is fixed at 0.6 mm for all designs.

The complete set of investigated designs is therefore as follows (see also Fig. 5):

(a) Matrix material with no IL (full design)
(b) Flat IL with $h = 0$ (flat design)
(c) Wavy IL with $\lambda = 6$ mm, $h = 4$ mm, $x_0 = 0$ (design 0)
(d) Reduced h: design 0 but $h = 2$ mm (low h)
(e) Increased h: design 0 but $h = 6$ mm (high h)
(f) Increased λ: design 0 but $\lambda = 10$ mm (high λ)
(g) Wave shifted by $\lambda/4$: design 0 but $x_0 = 1.5$ mm (shift $\lambda/4$)
(h) Wave shifted by $\lambda/2$: design 0 but $x_0 = 3$ mm (shift $\lambda/2$)

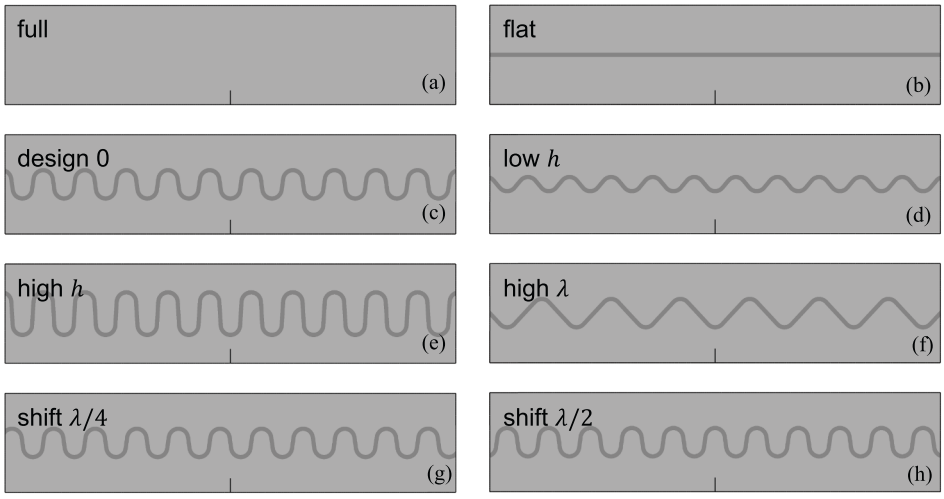

Fig. 5. The eight designs selected for the fracture bending experiments: a) full, b) flat, c) design 0, d) low h, e) high h, f) high λ, g) shift $\lambda/4$, h) shift $\lambda/2$.

2.2. Multi-material 3D printing of composite designs

The selected designs were prototyped using a commercial multi-material 3D printer (Objet260 Connex2) from Stratasys (USA). The printing process is based on the deposition of micrometer-sized droplets of a photopolymer ink through piezo-actuated nozzles at specified locations on a build platform. Each deposited layer is leveled to a uniform thickness of about 30 μm by a roller and subsequently cured by UV light with an intensity of 1780 mJ/cm^2. Concerning the printing speed, each layer is deposited and cured within approximately 10 s. By repeating this sequence layer-by-layer, the system can produce centimeter-scale objects [45]. The printer can operate simultaneously with two types of polymeric inks, enabling the fabrication of components with either elastomeric (Young's modulus at room temperature of 0.5–3 MPa [45,46]) or rigid (Young's modulus at room temperature of 1–3 GPa [45,47]) material behavior. Prior work by Zorzetto et al. [45] has shown that the printing orientation strongly influences the sharpness of the bi-material interface. To account for this anisotropy, the specimens were printed sequentially and vertically along the *x*-*z* axis to ensure consistent interface sharpness throughout the sample. All specimens were produced with a matte finish, meaning that all external surfaces were covered with support material to guarantee comparable surface quality.

2.3. Fracture testing

For the fracture mechanics investigation, the printed SENB specimens with the dimensions mentioned at the beginning of this chapter (Fig. 1a) were used. The initial notch was introduced at the center of each specimen, first by machine notching, followed by pre-cracking using a sharp razor blade. The razor blade notch was applied using a Leica RM2255 microtome (Leica Microsystems GmbH, Austria) through a gentle and uniform slicing motion up to a total a_0 of 2 mm.

Following notch preparation, the specimens underwent three-point bending tests. A universal testing machine (Zwick Z001, ZwickRoell GmbH & Co. KG, Germany) equipped with a 500 N load cell was employed. Deformation tracking and crack propagation monitoring were carried out via Digital Image Correlation (DIC) using a Basler boA6500-36 cm camera (Basler AG, Germany), equipped with a VST Lens VS-HX5035 F3.5 f50mm Super 35 from Basler AG (Germany). Prior to testing, specimens were prepared for DIC by applying a fine speckle pattern. Data analysis was performed using the Mercury RT system (Version 3.1, Sobriety s.r.o., Kuřim, Czech Republic), with an acquisition rate set to 25 frames per second. The radii of the fin and supports were 5 mm. The support span was 56 mm. The loading rate was kept constant at 10 mm/min throughout all experiments. For each pre-defined composite design, a total of three repetitions were conducted under laboratory conditions (23 °C and 50% r. h.).

Since fracture mechanics approaches are not applicable due to the presence of the compliant IL, and methodologies applied in previous studies (e.g., Refs. [9,12]) cannot be directly transferred due to the wavy nature of the compliant IL, global forces and energies were therefore investigated. The total energy absorbed during fracture, E_{tot}, was calculated via the area under the recorded force–displacement, $F(u)$, curve. By using this way of evaluation, it should again be noted that this value is not corrected by any calibration or geometry factor. As such, it provides a fracture parameter which is not intrinsic, i.e., geometry independent; nor is it generically associated with the two materials involved, nor can it be used to make comparisons with data reported in the literature, or obtained for other types of multi-material samples. Its purpose here is to investigate changes in E_{tot} among the different composite configurations analyzed.

For the calculation of S_0, a secant was fitted to the initial slope of the $F(u)$ curves response, between $u = 0.05$ and $u = 0.15$ mm, and its slope was then determined.

3. Results and discussion

3.1. Results of the parametric study

In the following, the results of the parametric study of h, r, and λ are presented. The IL thickness $t = 0.6$ mm is held constant and three setups concerning x_0 are considered: a) $x_0 = 0$ and no debonding, b) $x_0 = 0$ and debonding, and c) $x_0 = \lambda/2$.

Fig. 6 presents the $F(u)$ curves for λ of 6 mm. The colors blue, orange, green, and red indicate a h of 2 mm, 4 mm, 6 mm, and 8 mm, respectively. Within each diagram, dotted, dashed, and solid lines denote r values of 0.4 mm, 0.9 mm, and 1.4 mm, respectively. For comparison, a black curve represents the results obtained for the flat IL. The upper row (Fig. 6a-c) displays the complete $F(u)$ response up to ultimate failure, which occurs at u values of approx. 1.5 mm to 4.2 mm. The lower row (Fig. 6d-f) provides close-ups of the first peak in force of the same $F(u)$ curves to facilitate visualization of S_0 and F_c^0, as defined in Section 2.1.1. The columns of Fig. 6 differ with respect to x_0 and whether debonding is taken into account.

F_c^0 ranges from 60 N to 100 N and occurs at an applied displacement in the region of 0.22 mm for the wavy designs and 0.33 mm for the flat IL. F_c^1 depends strongly on x_0 and on whether debonding is considered. For $x_0 = 0$, debonding (compare Fig. 6a and Fig. 6b) leads to a pronounced reduction in stiffness immediately after F_c^0. Although the applied u at which F_c^1 occurs are similar with and without debonding, the substantially lower stiffness after F_c^0 results in a markedly reduced F_c^1 value. Consequently, the corresponding E_{tot} values are significantly lower when debonding is included. For $x_0 = \lambda/2$, the stiffness after F_c^0 lies between the two cases observed for $x_0 = 0$. However, the applied displacement at which F_c^1 is considerably lower than for $x_0 = 0$. This behavior can be explained by the fact that crack initiation occurs immediately after the arrested crack and at the beam's midspan, where the bending moment is maximal.

As mentioned above, r is represented by the line style in Fig. 6. It is evident that S_0 decreases slightly with increasing r, while F_c^1 exhibits a considerable decrease as r increases. This behavior is attributable to the notch effect, which governs the local stress concentrations and thus controls crack initiation from the IL. With respect to h, indicated by the line color in Fig. 6, the trends must be interpreted separately for the three cases of x_0 and the presence or absence of debonding. For the case of $x_0 = 0$ without debonding, both F_c^1 and E_{tot} increase with increasing h. In contrast, for the other two cases, the stiffness following F_c^0 as well as the F_c^1 decrease as h increases, while u at F_c^1 occurs increases with increasing h. Overall, E_{tot} decreases with increasing h for the case $x_0 = 0$ with debonding as well as for the case $x_0 = \lambda/2$.

The parameters S_0 and F_c^0 are shown in Fig. 6d-f as the initial slope and the height of the force peak, respectively. The influence of r on both S_0 and F_c^0 increases with larger h, whereas for $h = 2$ mm the curves nearly coincide. With respect to h, both S_0 and F_c^0 attain their highest values in the range of $h = 2$ mm to $h = 4$ mm, followed by a decrease, indicating that h can be optimized within this interval for the initial force response. Compared to the flat IL, represented by the black curve in Fig. 6, all wavy IL exhibit an increased S_0. F_c^0, however, exceeds that of the flat IL only for small values of h, and also depends on the specific case of x_0 and whether debonding is considered.

The $F(u)$ curves for $\lambda = 10$ mm are presented in Fig. 7 using the same way of visualization as in Fig. 6 for $\lambda = 6$ mm. The trends in the dependence of F_c^0, F_c^1 and S_0 on r and h are qualitatively the same as those observed for $\lambda = 6$ mm. However, for $\lambda = 10$ mm there is notably less variation in F_c^1 with h in the case of$x_0 = 0$ without debonding (Fig. 7a). This suggests that, with respect to ultimate failure, the ratio h/λ may be more relevant than the absolute value of h. The parameters S_0 and F_c^0 are less sensitive to r for $\lambda = 10$ mm than for $\lambda = 6$ mm and exhibit maximum values in the range of $h = 4$ mm to $h = 6$ mm, further

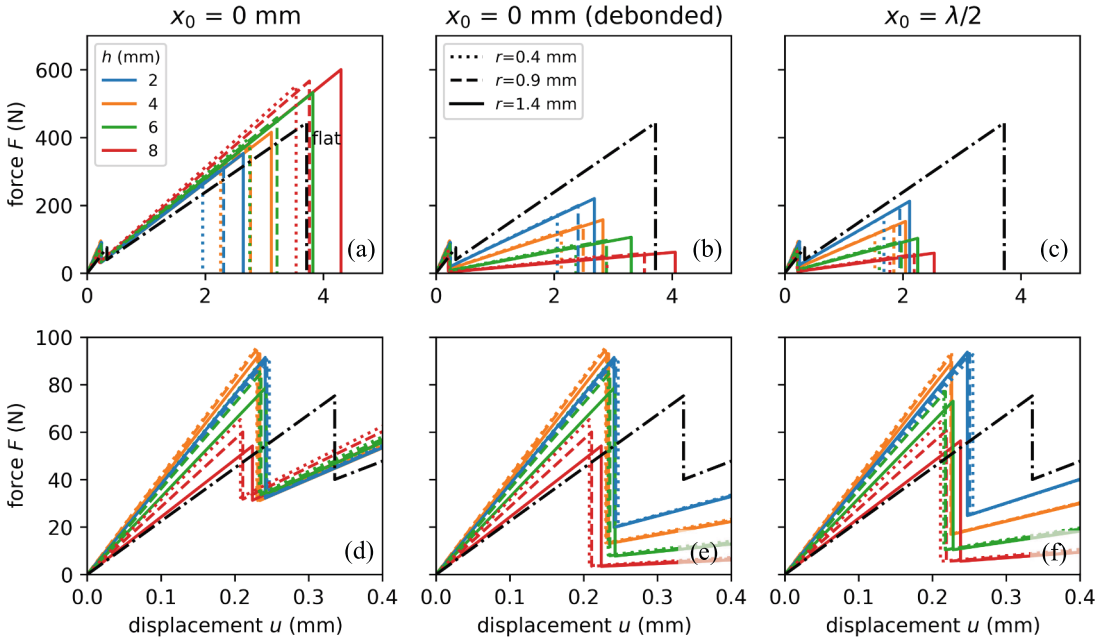

Fig. 6. $F(u)$ curves of the parametric study with $\lambda = 6$ mm and varied h and r, with the complete $F(u)$ curves in the upper row and a close-up of the first drop in force in the lower row. The columns indicate results for $x_0 = 0$ (a, d), $x_0 = 0$ with debonding (b, e), and $x_0 = \lambda/2$ (c, f). The legends in (a, b) refer to the entire figure. The color coding indicates variations in h, while the line style represents variations in r. In Addition, the flat configuration is shown in black with a dash–dot line style.

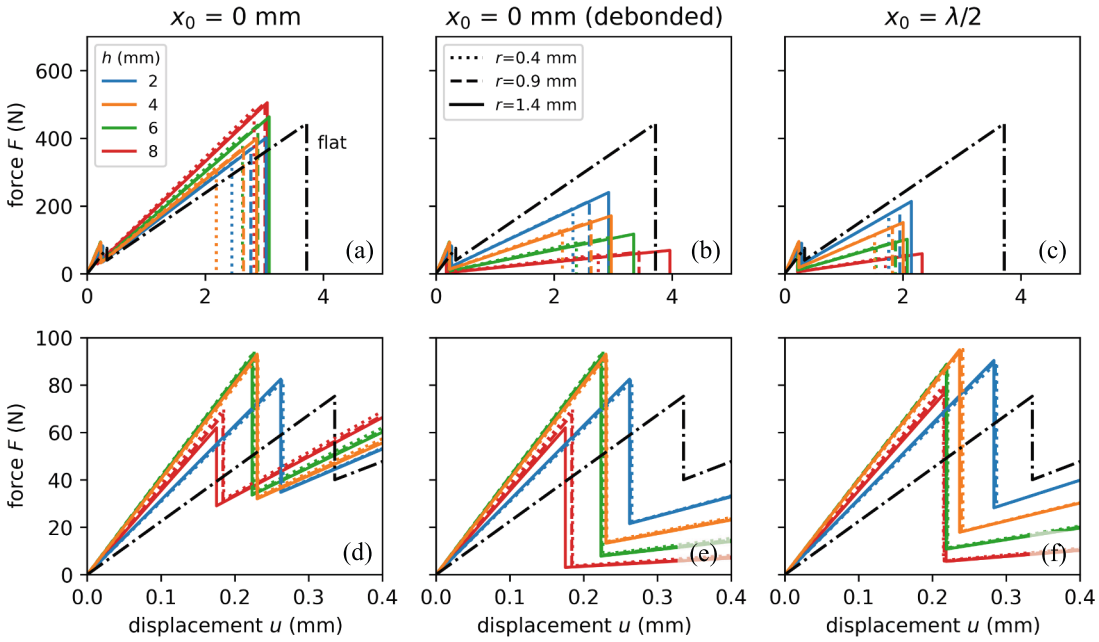

Fig. 7. $F(u)$ curves of the parametric study with $\lambda = 10$ mm and varied h and r, with the complete $F(u)$ curves in the upper row and a close-up of the first drop in force in the lower row. The columns indicate results for $x_0 = 0$ (a, d), $x_0 = 0$ with debonding (b, e), and $x_0 = \lambda/2$ (c, f). The legends in (a, b) refer to the entire figure. The color coding indicates variations in h, while the line style represents variations in r. In Addition, the flat configuration is shown in black with a dash–dot line style.

indicating a dependence on the ratio h/λ.

In the h,r study presented before, E_{tot} generally increases with increasing r, whereas S_0 decreases only slightly as r increases. For certain applications in which both E_{tot} and S_0 should be maximized, r should therefore be chosen as high as possible. Consequently, in the following study, r is fixed at its highest previously examined value of 1.4 mm, while h is varied between 0 (flat IL) and 8 mm, with a higher density of data points towards $h = 0$. This analysis is conducted for both $\lambda = 6$ mm and $\lambda = 10$ mm.

Fig. 8 presents S_0 (a), and F_c^0 (b), and E_{tot} (c) as functions of h/λ for $\lambda = 6$ mm (cyan curves) and $\lambda = 10$ mm (magenta curves). The line styles indicate the respective cases of x_0 and the consideration of debonding.

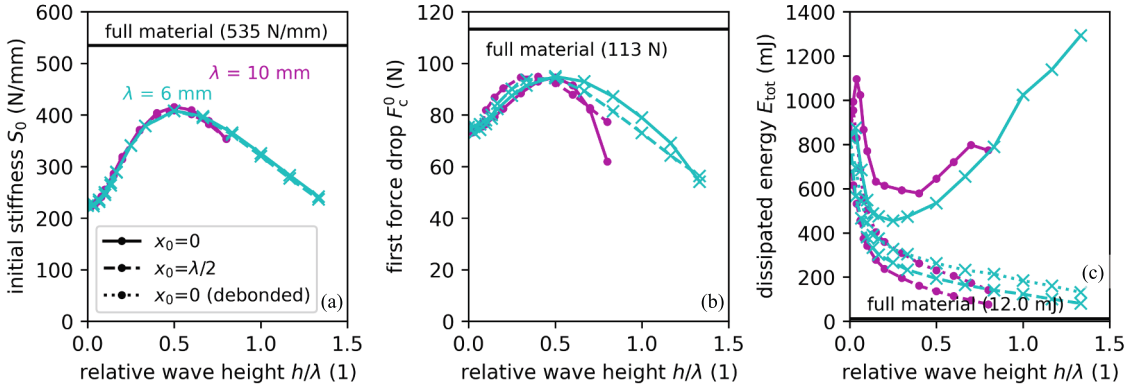

Fig. 8. Computed values of (a) initial stiffness, S_0, (b) force for first crack propagation, F_c^0, and (c) total dissipated energy, E_{tot}, for varied relative wave heights h/λ but fixed $r = 1.4$ mm and $\lambda = 6$ mm (cyan curves and x markers) and $\lambda = 10$ mm (magenta curves and circle markers). A h/λ of 0 corresponds to a flat IL. Curves for the full material are plotted in black for reference. (For interpretation of the references to colour in this figure legend, the reader is referred to the web version of this article.)

All curves coincide at $h/\lambda = 0$, which corresponds to a flat IL configuration. For reference, the response of the full material is shown by the black curves, providing baseline values for S_0, E_{tot}, and F_c^0. In addition, it should be noted that the number of computed data points differs between $\lambda = 6$ mm and $\lambda = 10$ mm, which is related to the geometric constraints of the specimen, resulting in a higher number of feasible configurations for $\lambda = 6$ mm. Accordingly, a fully dimensionless analysis is hindered for $h/\lambda > 0.8$ in the case of $\lambda = 10$ mm, where the IL waves come too close to the specimen's surface.

S_0 is approx. 535 N/mm for the full material and drops to 224 N/mm for the flat IL ($h/\lambda = 0$). For both λ values, the S_0 curves for $x_0 = 0$ and $x_0 = \lambda/2$ nearly coincide. The highest S_0 values occur at $h = 3$ mm ($h/\lambda = 0.5$) and $h = 5$ mm ($h/\lambda = 0.5$) for $\lambda = 6$ mm and $\lambda = 10$ mm, respectively. These maxima are about 25% lower than S_0 of the full material, while S_0 of the flat IL is reduced by about 60% relative to the full material. F_c^0, which is 113 N and 73.5 N for the full material and flat IL, respectively, also reaches a maximum within a similar range of h/λ as observed for S_0. However, the location of this maximum depends on x_0. For $x_0 = 0$, the maximum is shifted toward to larger h/λ values compared to $x_0 = \lambda/2$, which is more pronounced for $\lambda = 10$ mm.

E_{tot} is 12 mJ for the full material and increases to 830 mJ for the flat IL. For $x_0 = 0$ without debonding, E_{tot} initially rises with increasing h/λ, reaching maxima of 875 mJ for $\lambda = 6$ mm and 1096 mJ for $\lambda = 10$ mm. Thereafter, it drops to a minimum of 455 mJ at $h/\lambda = 0.25$ for $\lambda = 6$ mm and 579 mJ at $h/\lambda = 0.4$ for $\lambda = 10$ mm, before increasing again at larger h/λ values. While E_{tot} for $x_0 = 0$ without debonding continues to increase for large h/λ values in the case of $\lambda = 6$ mm, it decreases from $h/\lambda = 0.7$ to $h/\lambda = 0.8$ for $\lambda = 10$ mm. When debonding is included for $x_0 = 0$, the initial rise in E_{tot} disappears for $\lambda = 6$ mm and is reduced for $\lambda = 10$ mm, where a maximum of 955 mJ is obtained. Beyond this point, E_{tot} for $x_0 = 0$ with debonding decreases monotonically as h/λ is increased. For $x_0 = \lambda/2$, no initial increase is observed. Instead, E_{tot} decreases monotonically with increasing h/λ, following a similar trend as for $x_0 = 0$ with debonding but at lower values. For the sake of completeness, it should be emphasized that all configurations incorporating an IL exhibit E_{tot} values that are substantially higher than that of the full material ($E_{tot} = 12$mJ).

Fig. 9a and b plot E_{tot} against S_0 for the study with varying h. Starting at $h = 0$, corresponding to the flat IL and marked by an "x", the size of circular markers indicates the value of h. The color code follows that of Fig. 8, distinguishing between the cases of x_0 and the presence of debonding. Another black "x" marker denotes E_{tot} over S_0 for the full material.

The diagrams in Fig. 9 summarize the overall effects of incorporating a compliant IL in bending beams. The full material exhibits high S_0 but

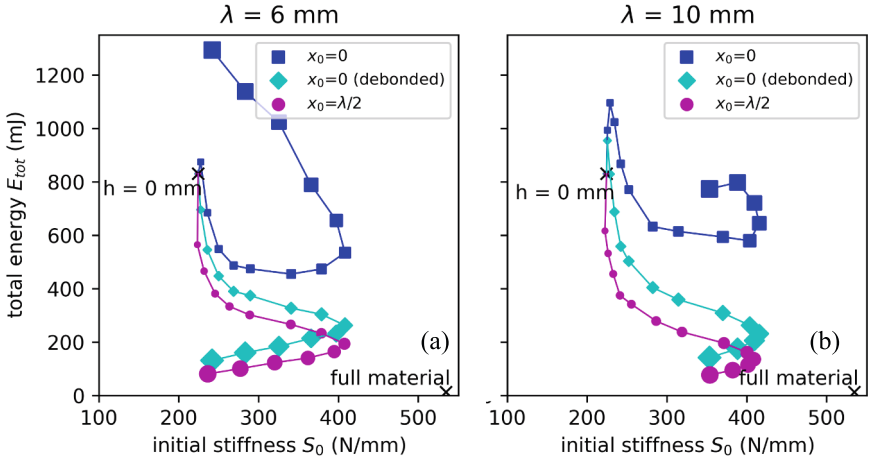

Fig. 9. Results of the h study with $r = 1.4$ mm in terms of plotted total dissipated energy, E_{tot}, over initial stiffness, S_0, for a) $\lambda = 6$ mm and b) $\lambda = 10$ mm. Curves for $x_0 = 0$, $x_0 = 0$ with debonding, and $x_0 = \lambda/2$ are plotted in blue, cyan, and magenta, respectively. The size of the markers indicates the wave height h. (For interpretation of the references to colour in this figure legend, the reader is referred to the web version of this article.)

an extremely low E_{tot}. Introducing a flat IL ($h = 0$) considerably increases E_{tot}, albeit at the expense of a roughly 60% reduction in S_0. Employing a wavy IL, S_0 can be increased again, but may also cause a decrease in E_{tot} relative to the flat IL.

Differences arising from x_0 and from the inclusion of debonding are also visible in Fig. 9. Considering that a complete absence of debonding is unrealistic, a practical design region for h can be identified between $h = 0$ and h with the highest S_0. Depending on design requirements, whether high stiffness or high energy dissipation is prioritized, a suitable wave height h can thus be selected.

3.2. Fracture testing

3.2.1. Deformation and fracture process description

Fig. 10 illustrates deformation and crack propagation in the eight selected designs. The images outlined in red show the crack state immediately after initiation, while those in blue show the crack shortly before complete fracture. The green crosses indicate the position of final fracture. Fig. 11 presents the $F(u)$ curves from the fracture experiments (one representative curve per design, based on three repetitions).

For the design full, it was observed that after reaching F_c^0, the crack initiates and subsequently propagates unstably through the entire specimen. The corresponding $F(u)$ response in Fig. 11 indicates brittle behavior, which is further confirmed by the SEM images of the fracture surface presented in the supporting information. In addition to the SEM images, a video (Fracture_full.mp4) is provided as supplementary data, which illustrates the fracture process. However, such fracture characteristics are typical for glassy photopolymers or cured resins in general [12,48,49]. In addition, S_0 exhibits the highest value for the full design compared to the other investigated design variants, while E_{tot} remains comparatively low.

With the incorporation of a compliant IL, as for the design flat, the fracture behavior and the associated mechanical characteristics change drastically. The crack initiates abruptly and in a brittle manner at a significantly lower F_c^0 (Fig. 11) and is directly driven into the compliant IL. This effect, known as anti-shielding effect [50,51], has previously been observed in different multi-material resin systems by, e.g., Schwaiger et al. [12] or Waly et al. [27]. As deformation progresses, the crack continues to propagate straight through the IL until it reaches the compliant-to-stiff interface, where it is arrested due to the material inhomogeneity effect and the corresponding reduction in local CDF [6–8]. In contrast to the stiff-to-compliant transition, a shielding effect occurs at this position, which essentially arises from the spatial variation of the mechanical properties of the constituent materials [50,51]. With increasing deformation, the crack starts to deflect into the stiff-to-compliant interface. A detachment of the compliant IL from the matrix material is observed, which is shown in the microscopic images in the supporting information. Additionally, a video (Fracture_flat.mp4) showing the fracture process is provided as supplementary data. In combination with the bending of the remaining undamaged ligament, which progressively undergoes plastic deformation with increasing displacement. Final failure occurs only after the critical bending stress is reached at the location of maximum bending moment. SEM images shown in the supporting information illustrate the crack sensitivity of the matrix material in the design flat. In the region of crack initiation, the fracture surface appears brittle, whereas the fracture surface of the residual ligament shows pronounced plastic deformation, supporting the observation of significant energy absorption. Compared to the design

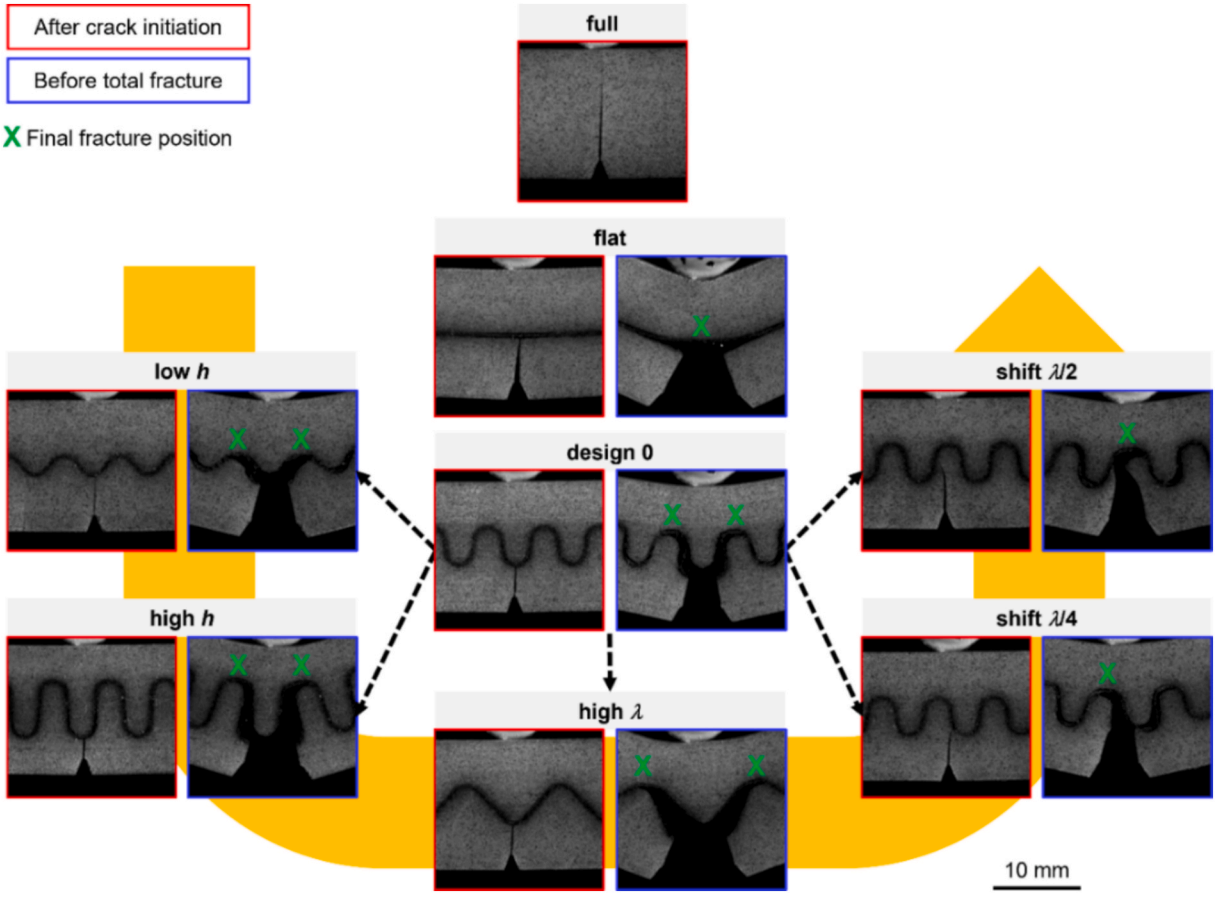

Fig. 10. Deformation and fracture behavior of 3D printed composite beams (selected configurations). Images outlined in red show the crack immediately after initiation, those outlined in blue depict the crack shortly before ultimate fracture. The green crosses indicate the position of final fracture. (For interpretation of the references to colour in this figure legend, the reader is referred to the web version of this article.)

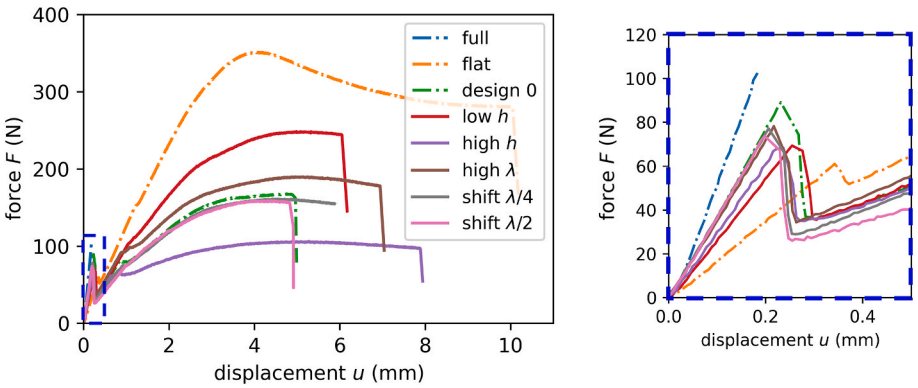

Fig. 11. $F(u)$curves of the investigated composite designs obtained from the fracture experiments. The blue dash-dotted box highlights a detailed view of the deformation range up to $u = 0.5$ mm. The key designs (full, fat, design 0) are presented in dash-dotted lines. (For interpretation of the references to colour in this figure legend, the reader is referred to the web version of this article.)

full, however, E_{tot} is considerably higher for specimens with IL, while both F_c^0 and especially S_0 are substantially lower. This pronounced reduction in S_0 can essentially be attributed to stress decoupling, induced by the incorporation of the compliant IL [9]. Because of this effect, only limited stresses can be transmitted across the compliant IL under initial loading, which ultimately leads to the decrease in S_0. The low S_0 is directly linked to the reduced measured F_c^0. Assuming identical notch conditions (a_0 and notch-tip radius), the larger deformation of the cracked ligament results in a higher local stress concentration at the crack tip (at the same applied forces), which in turn inevitably promotes earlier crack initiation.

When considering design 0 and its derived variants (low h, high h, and high λ), a different deformation and fracture behavior emerges compared to the previously discussed designs. Initial crack growth proceeds abruptly and in a brittle manner up to the wave trough, as evidenced both by the $F(u)$ curves in Fig. 11 and the fracture surfaces presented in the supporting information. The crack then moves into the compliant IL, where it propagates symmetrically with increasing deformation. From this point onward, however, the crack growth behavior differs substantially from that of the flat design. Instead of simply penetrating the compliant IL, the wavy geometry introduces a more complex stress state, leading to partial delamination at the interfaces and visible deformations induced by shear, tensile, and compressive forces. This complex crack progression, together with bending of the undamaged residual ligament, results in energy absorption levels that fall between the two reference designs, full and flat. A video of the fracture processes of the different designs (Fracture_design0.mp4, Fracture_low_h.mp4, Fracture_high_h.mp4 and Fracture_high_lambda.mp4) is provided as supplementary data. Compared to the design full, E_{tot} is considerably higher, which can be attributed to the compliant IL and its crack-arresting effect. Relative to the design flat, however, E_{tot} is consistently lower, which can be explained by two main factors. First, the presence of the wave structures reduces the residual ligament, thereby limiting load-bearing capacity and associated energy dissipation during deformation. Second, the curvature of the wave peaks introduces stress concentrations (depending on radii [52,53]), which promote premature failure at these locations (Fig. 10) with less plastic deformation at failure compared to the design flat (more details can be found in the supporting information). S_0, likewise falls between the two reference designs. Compared to the design full, S_0 is lower due to the compliant IL and the associated stress decoupling. However, it remains noticeably higher than that of the design flat, owing to the more complex stress state that arises in the wavy IL under initial loading. This effect is also reflected in F_c^0, which is higher than in the flat design due to the increased overall specimen stiffness.

When the wave is shifted horizontally relative to the initial notch, as in the designs shift $\lambda/2$ and shift $\lambda/4$, the crack growth after initiation becomes asymmetric, yet retains the same level of complexity as in design 0 and its parametric variations. A video of the fracture process (Fracture_shift_lambda_2.mp4 and Fracture_shift_lambda_4.mp4) is provided as supplementary data. In these cases, the crack propagates along the wave crest, where failure ultimately occurs with increasing bending of the residual ligament. However, the particularly interesting aspect of these designs lies not in the crack propagation behavior within the compliant IL, but in the crack initiation step. In the case of design shift $\lambda/4$, where the offset between the wave and the initial notch is relatively small, the crack is not directed straight toward the IL but is instead deflected toward the wave trough, which fits well with the simulation results. For design shift $\lambda/2$, where the notch would theoretically be positioned directly below the wave crest, a similar deflection occurs, since achieving an exact alignment of the notch under a wave peak is practically unfeasible.

Regarding the influence of printing-induced microstructure on the deformation or fracture behavior observed, it should be noted that all repeated tests exhibited highly consistent results with only minor scatter in S_0 and F_c^0 (illustrated in Section 3.2.2). Moreover, the SEM images, presented in the supporting information, reveal no evidence of pores or defects typically associated with printed structures, like, e.g, in material extrusion [54] technique.

3.2.2. *Influence of wave parameters on* F_c^0, S_0 *and* E_{tot}

Having established the deformation and fracture behavior of the selected designs, it remains to be clarified to what extent the wave parameters influence the parameters of interest (F_c^0, S_0 and E_{tot}) in the fracture tests and how significant these effects are. In Fig. 12 these values are shown for all pre-selected designs. Fig. 12a presents S_0 and F_c^0 compared, and Fig. 12b presents S_0 and E_{tot} compared.

With respect to Fig. 12a, the data demonstrate that the introduction of a compliant IL invariably results in its reduction in S_0. The underlying reason is stress decoupling caused by the compliant IL, which transmits only limited stresses. Consequently, wavy IL configurations, such as in design 0, are advantageous compared to a flat IL (as in design flat), since the wavy geometry induces a more complex stress state, thereby mitigating the reduction in S_0. As previously mentioned, design 0 was preselected due to its highest S_0 value. Any deviation in h, for example, leads to a reduction in S_0, as observed in both the low h and high h design. While the difference between these two designs appears small, it is nonetheless statistically significant within a 95% confidence interval. This can primarily be explained by the stress state in the compliant IL, which is expected to be substantially more complex in the design high h. Interestingly, λ appears to have little to no significant effect on S_0 relative to design 0, which is consistent with the findings of the parametric study, at least for the selected $h = 4$ mm for design 0. For larger or

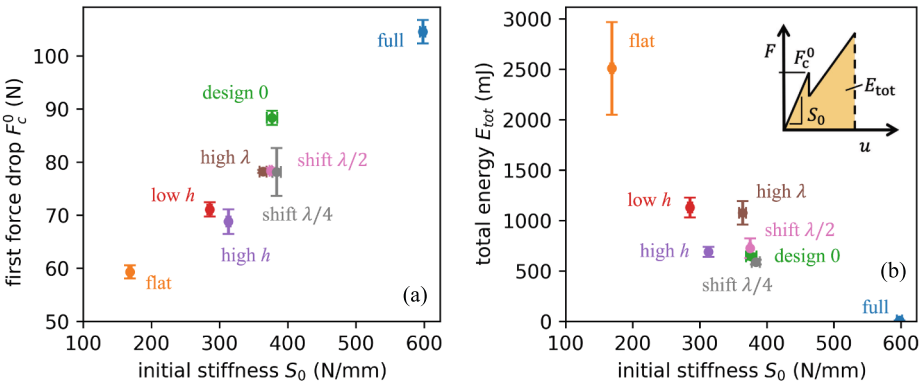

Fig. 12. Results from the fracture experiments of the eight selected designs. (a) presents the results of the critical force for crack initiation, F_c^0, and the initial stiffness, S_0, compared, (b) the results of the total dissipated energy, E_{tot}, and S_0, compared.

smaller values of h, however, a significant influence on the investigated parameters can be observed (Fig. 8).

Similarly, initial crack positioning seems to have a negligible influence on S_0, as evidenced by the comparison between design 0 and the design shift $\lambda/2$ and shift $\lambda/4$. This outcome is given by the fact that the geometric characteristics of the IL remain unchanged. In contrast, F_c^0 exhibits significantly lower values in the shifted designs, which can be attributed to the asymmetric loading conditions at the crack tip.

At this point, it should be noted that, in addition to the fracture experiments, mechanical tests in the form of three-point bending experiments were also conducted to assess the stiffness of the designs in the absence of a crack. These results are not part of the main study and can be found in the supporting information. A comparative assessment shows that the mechanical and fracture experiments exhibit the same trends with respect to stiffness response, which further indicates that crack introduction was performed consistently.

As can be seen in Fig. 12b, the introduction of a compliant IL consistently leads to an increase in E_{tot} due to the crack-arresting effect, regardless of the IL geometry. Moreover, a clear trend emerges with respect to E_{tot} and the choice of IL shape. This trend can essentially be attributed to the interplay of three factors: (I) the contribution of the remaining undamaged ligament after the crack has reached the second interface, (II) the presence of stress concentrations induced by r at possible wave peaks and (III) the specific geometry of the compliant IL itself, which directly governs the additional surface area released during crack progression; this process also requires energy.

When considering the design flat, a substantial increase in E_{tot} compared to the design full is observed. This increase can primarily be attributed to the bending of the relatively thick remaining ligament, which does not experience additional stress concentrations from a wavy structure and can therefore be loaded in a manner comparable to a single, uncracked, decoupled bending beam. The contribution of energy dissipation due to delamination at the interface in this case is expected to be negligible, since the IL undergoes no complex deformations. Thus, the main source of energy absorption is the bending of the remaining ligament. When a wavy IL is embedded instead, as in the case of design 0, the thickness of the remaining ligament is locally reduced, thereby lowering the overall capacity to absorb energy. In addition, the radii at the wave peaks introduce stress concentrations, which can promote premature failure and further reduce E_{tot}. Although the stress state within the IL becomes more complex, involving not only penetration and delamination but also substantial deformation (see also supporting information), this effect cannot compensate for the reduced ligament thickness and the stress concentrations at the wave peaks, since the mechanical properties of the compliant IL remain inferior to those of the stiff matrix.

When h is reduced, as in design low h, E_{tot} increases significantly compared to design 0. This increase can be explained by the enlargement of the remaining undamaged ligament, which allows the specimen to sustain higher stresses at larger deformations and thus enhances energy absorption. Conversely, increasing h (design high h) locally reduces the ligament thickness but at the same time generates a more complex stress state within the IL under the applied bending. In this case, shear stresses within the IL, as well as tensile stresses acting at the interface (necessary to promote IL debonding) play a more dominant role. As a result, no significant difference in E_{tot} was observed when compared to design 0.

A similar rationale can be applied to interpret the influence of λ. In this case, a clear increase relative to design 0 is observed. While the ligament thickness and stress concentration effects due to the radii remain essentially unchanged, the stress state within the IL and at the interfaces becomes more severe as a result of the larger λ and the associated flatter wave crest. Under bending, the opening of the flanks induces tensile stresses along the interfaces. The separation of the IL from the matrix requires additional energy, which in turn increases E_{tot}.

The initial crack position, as varied in designs, shift $\lambda/2$ and shift $\lambda/4$, shows negligible influence on E_{tot}. For shift $\lambda/2$, slightly lower values than design 0 are observed, whereas shift $\lambda/4$ exhibits a slight increase. However, these deviations are not statistically significant. Minor variations can primarily be attributed to asymmetric loading conditions and the corresponding differences in crack propagation.

As shown by the presented data, the investigated parameters F_c^0, S_0 and E_{tot} can be tailored to the requirements of a specific application through the incorporation of a compliant IL. When high toughness is critical, for example, the flat design may be employed. Compared to the design full, this configuration increases E_{tot} by a factor of approx. 300 (30000%), but at the cost of a substantial reduction in S_0 by over 70%. Since cracks can often initiate during service, and early crack propagation needs to be mitigated, wavy IL designs provide a compromise. In the case of design 0, E_{tot} increases by a factor of roughly 80 (8000%) relative to the full design, while reductions in S_0 and F_c^0 are significantly smaller, around 40% for S_0. These results underscore that the use of a compliant IL necessarily involves trade-offs. None of the three parameters can simultaneously surpass the advantages offered by the reference designs, full or flat. Nevertheless, the wavy IL concept demonstrates that, by tuning geometric parameters (including variations in t and r), the number and position of layers, and other design variables, the mechanical or fracture response can be deliberately optimized for specific application requirements.

3.3. Comparison of numerical and experimental results

As previously outlined, the objective of this study is the development of a model that enables a rapid screening of wavy IL structures, with a

particular focus on the parameters F_c^0, S_0 and E_{tot}. Of these, F_c^0 and S_0 are of particular relevance, since cracks may arise during service and their propagation depends strongly on the geometric characteristics of the wavy IL, which in turn directly influence the overall structural stiffness. Due to the chosen material combination and the effect of material inhomogeneity, an increase in E_{tot} is consistently observed. Whether such an increase by several orders of magnitude is required, remains application-dependent. In any case, E_{tot} is governed primarily by the geometric configuration of the remaining ligament after crack initiation and the subsequent crack propagation through the compliant IL.

Fig. 13 presents a comparison between numerically predicted and experimentally measured data. Fig. 13a-c illustrates the complete deformation response up to fracture for the different investigated designs, while Fig. 13d-f provides a magnified view of the region of interest up to a displacement of $u = 1.5$ mm. As evident from the results, the simulated and experimental $F(u)$ curves exhibit marked differences in the region following the initial crack initiation and subsequent failure up to fracture. The assumption of linear-elastic material behavior after crack initiation employed in the numerical models does not adequately represent the actual deformation response of the specimens under increasing deformations. This is also illustrated in Fig. 13, where the triangles in the simulated $F(u)$ curves indicate the estimated onset of plastic deformation based on the experimental results. The estimation was derived from the tensile test data provided in the supporting information. From the tensile curves of VW+, a stress level of approximately 40 MPa was identified as the point where plastic deformation begins to play a role. To determine when plastic deformation becomes relevant for the specimen deformation, the regions near the roller contact and the crack tip were excluded, as they would yield at relatively low loads. Instead, the maximum von Mises stress in the matrix near the compliant-to-stiff interface was evaluated. Based on this stress, the applied displacement in the numerical models was scaled to determine u corresponding to plastic deformation onset. As shown in Fig. 13, plastic deformation already begins to play a role at relatively small u, in the range of approximately 0.75 – 1.5 mm. This also explains why the simulated and experimental $F(u)$ responses start to diverge shortly after crack initiation and depends on whether debonding is considered or not.

However, this observation is further supported by Fig. 14, where the parameters of interest from the numerical and experimental results are plotted against each other. In particular, Fig. 14a highlights the deviations between simulated and experimental values of E_{tot}. Except for design 0, the agreement between experimental and numerical results is reduced, as indicated by the increased deviation of the data points from the dashed 45° line. In particular, the design flat exhibits substantial deviations, which are also apparent from the corresponding $F(u)$ responses. The good agreement observed for design 0 is considered coincidental, as can likewise be inferred from the $F(u)$ responses. In this context, more advanced material models are required to capture the real material behavior with higher accuracy. Furthermore, the modeling of crack propagation through the compliant IL leaves considerable scope for future investigations, an area that is currently under active research. Future models that consider the effects of IL/matrix debonding and the elastic–plastic matrix material can provide a detailed understanding of their role. However, this poses a challenge regarding computational cost because the non-linearity does not permit the load scaling used in this study.

Nevertheless, when focusing on the crack initiation regime (Fig. 13d-f) and the associated F_c^0 and S_0 values shown in Fig. 14b and Fig. 14c, respectively, it becomes evident that the linear-elastic model reproduces the material response with good fidelity. As mentioned previously, this

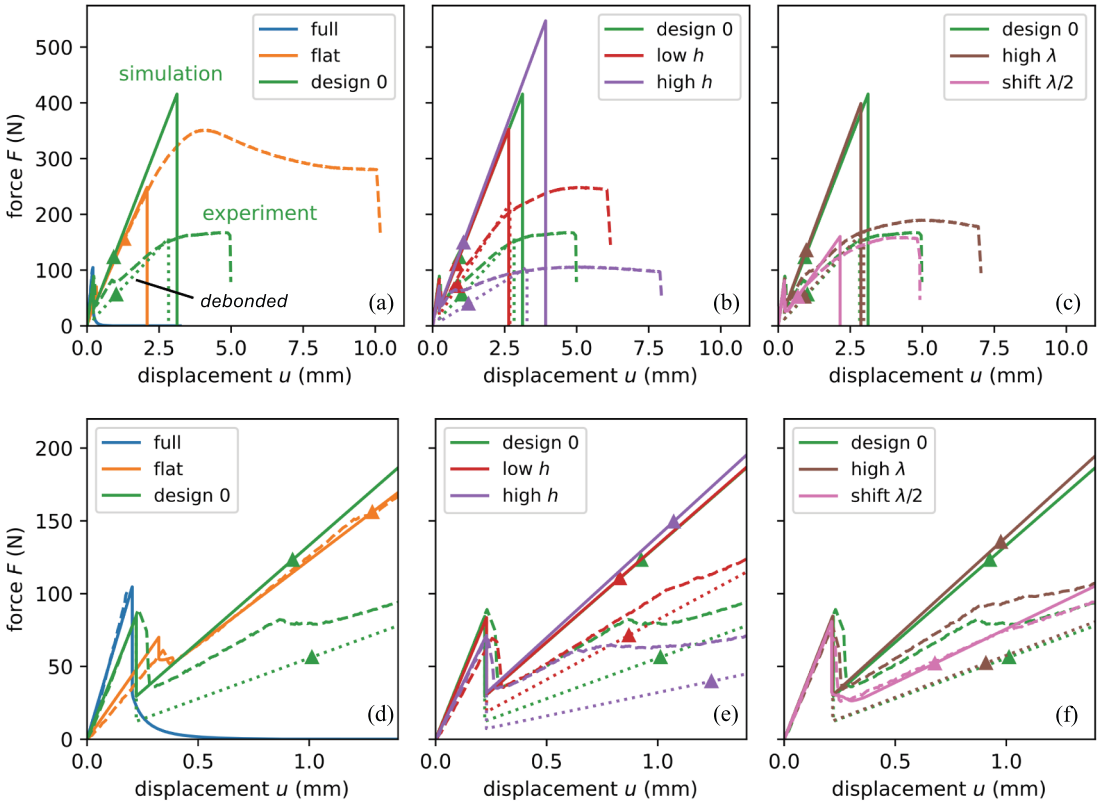

Fig. 13. Comparison between numerically predicted and experimentally measured data. (a) – (c) illustrates the comparison of the complete $F(u)$ curves up to fracture, while (b) – (f) provides a magnified view of the region of interest for displacements up to $u = 1.5$ mm. Solid lines show the simulation results, dashed lines represent the experimental data, and dotted lines indicate cases where debonding was considered. The predicted onset of plastic deformation is marked by triangles.

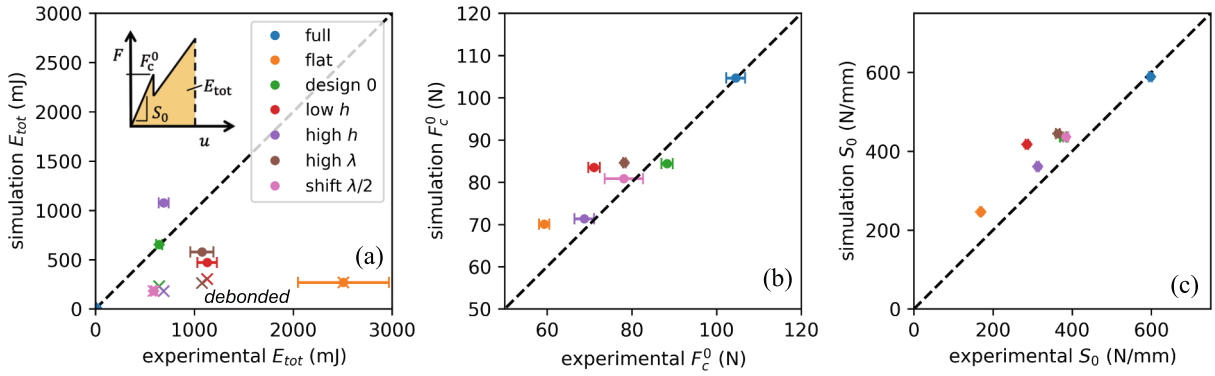

Fig. 14. Comparison between numerically predicted and experimentally measured data. Panels (a–c) present a direct comparison of the numerically predicted and experimentally measured mechanical quantities of interest, with the dashed 45° line indicating perfect agreement between simulation and experiment. The crosses in (a) indicate the results where debonding was included in the numerical simulations.

regime is of particular relevance for the present study. Both the absolute values, reflected by the proximity to the 45° line, and the trends of F_c^0 and S_0 exhibit close agreement between numerical predictions and experimental data, demonstrating that the model is well suited for rapid pre-selection of designs tailored to applications with known loading scenarios. With respect to the geometric parameter h, starting from the design flat, an increase in F_c^0 and S_0 is observed with increasing h (low h), followed by a further increase leading to a maximum for design 0, and a subsequent decrease for larger values of h (high h). This trend is in good agreement with the numerical results presented in Fig. 9. Regarding λ, an equally good agreement between numerical and experimental investigations is observed. For $\lambda = 6$ mm (design 0) and $\lambda = 10$ mm (high λ), no significant difference in F_c^0 and S_0 is observed for the considered h of 4 mm, as shown in Fig. 14b and Fig. 14c and corroborated by Fig. 8. However, it shoul be emphasized, that this observation does not imply an absence of influence of λ on F_c^0 and S_0, as clearly demonstrated in Fig. 8. Rather, the specific IL geometry of the samples pre-selected for experimental investigations represents a limiting case in which, for a h of 4 mm, F_c^0 and S_0 attain nearly identical values. A shift of the wave by shift $\lambda/2$ or shift $\lambda/4$ does not result in a significant variation in F_c^0 and S_0, neither numerically nor experimentally. Only the crack propagation path itself is affected, as illustrated in Fig. 10, leading to an asymmetric crack growth through the sample.

Finally, it is essential to note that this study is subject to several boundaries and limitations. The experiments were conducted under quasi-static loading conditions. Therefore, the observations are valid only for this specific condition. No direct conclusions can be drawn for other loading scenarios, such as fatigue or long-term loading. The same is true for environmental and testing conditions. Variations in temperature or loading rate may alter the behavior of the constituent materials, owing to the temperature- and strain-rate sensitivity of polymeric materials [55], and consequently affect the failure mechanisms. The chosen material combination further plays a decisive role in the fracture behavior. In general, the response is governed by the interplay between the fracture toughness of the compliant IL and that of the formed interface (strong or weak) between dissimilar materials [56]. If both the IL and the interface exhibit high toughness, the IL is not penetrated but undergoes plastic deformation, while the crack initiates within the stiff matrix ligament, as shown, for instance, by Wiener et al. [9,13] in a PP multi-layer system. In contrast, if the IL exhibits high toughness but the interface is weak, the effect of material inhomogeneity becomes almost negligible. The crack deflects into the interface, resulting in delamination without penetrating the IL [57]. This mechanism of fracture toughness enhancement must therefore be considered independently of the material inhomogeneity effect. If, however, the interface is strong compared to the compliant IL, the situation observed in the present study arises. The crack penetrates the IL, is arrested due to the material inhomogeneity effect, and subsequently deflects. Such behavior has been repeatedly reported in various resin-based systems [12,27]. It should be noted, however, that these insights from the literature are predominantly based on flat IL geometries. When the IL becomes wavy, the more complex stress state within both the IL and the interface can give rise to intricate failure mechanisms involving plastic deformation, debonding, and penetration. Capturing these effects accurately requires further numerical and experimental investigations. In the current models, such mechanisms are only partially and in a simplified manner represented, which constitutes an important limitation of the present study.

4. Summary and Conclusion

Inspired by the wide variety of geometric patterns found in the Earth's lithosphere, the present study aimed to investigate the potential for mechanical property enhancement by embedding a compliant, symmetric wavy interlayer (IL) into a stiff matrix. The overarching motivation was to overcome the principal drawback of flat ILs, namely the stress decoupling and the resulting loss in structural stiffness, which inevitably occurs as different designs are implemented to increase fracture resistance. Given the large number of geometric parameters that may influence the fracture properties of wavy ILs, such as IL thickness, t, wave radius, r, wave height, h, wavelength, λ, and the initial crack position, x_c, relative to the IL, a numerical approach was adopted prior to experimental investigation. In the design-oriented numerical models, t and r were held constant, while h, λ, and x_c were systematically varied within predefined ranges. Particular attention was given to the force–displacement curves and the corresponding quantities of interest, the initial stiffness prior to crack initiation, S_0, the force required for first crack initiation, F_c^0, and the total energy dissipation, E_{tot}. Based on the simulation results, a reference design (design 0) offering highest S_0 while maintaining a high E_{tot} was selected. Subsequently, variations in h, λ, and x_c were derived from this reference configuration. Overall, seven designs were then fabricated via PolyJet 3D printing using VW+ as the stiff matrix material and TB+ as the compliant IL. These designs were then tested in fracture experiments using a three-point bending arrangement.

The following conclusions were drawn:

- Numerical and experimental findings demonstrate that embedding a compliant IL within a stiff matrix significantly increases E_{tot}, but reduces S_0 and F_c^0.
- Using a wavy IL, instead of a flat one, partially restores S_0 and F_c^0, but yet decreases E_{tot} caused by stress concentrations at the wave peaks and the geometrically induced reduction of the remaining

undamaged ligament. Therefore, a certain trade-off between S_0/F_c^0 and E_{tot} appears unavoidable.
- As demonstrated experimentally, reducing h increases E_{tot} but decreases S_0 and F_c^0, while the influence of λ was observed to be negligible.
- Although shifting the wave leads to asymmetric crack propagation, the effect of x_c on the overall results is negligible.
- Numerical and experimental results agree well (for F_c^0 and S_0) as long as the structural response remains nearly linear-elastic, but deviate beyond F_c^0 due to non-linear material behavior, interface debonding, and the complex deformation and damage mechanisms occurring within the compliant IL during the fracture process.
- The numerical model is suitable for rapid preliminary design screening, while still highlighting the need for significant future work to more accurately capture real deformation and fracture behavior.

Overall, the present investigation demonstrates that embedding a wavy IL provides an effective way to tailor the (fracture-)mechanical response of polymeric multi-layer composites, enabling a balanced compromise between energy dissipation and stiffness retention. But the concept also offers substantial space for further research activities. Future work may focus, for example, on identifying or adapting suitable manufacturing routes to enable large-scale implementation of such architectures in real structural parts, like pipes or plates. Moreover, the wide variety of lithospheric fold geometries offers considerable potential for exploiting additional stiffness-enhancing mechanisms, such as geometric interlocking. Building on this, it will be particularly relevant to examine how the integration of multiple compliant ILs, as well as their arrangement to each other, further affects damage tolerance and stiffness, and how such composites behave under long-term and cyclic loading.

CRediT authorship contribution statement

Christoph Waly: Writing – original draft, Visualization, Validation, Methodology, Investigation, Conceptualization. **Martin Pletz:** Writing – original draft, Visualization, Validation, Supervision, Methodology, Investigation, Conceptualization. **Tim Volders:** Writing – original draft, Visualization, Methodology, Investigation. **Marco Contino:** Writing – review & editing, Validation, Methodology. **Federico Passoni:** Writing – review & editing, Validation, Methodology. **Davide Ruffoni:** Writing – review & editing, Supervision, Resources, Methodology. **Luca Andena:** Writing – review & editing, Supervision, Methodology. **Florian Arbeiter:** Writing – review & editing, Supervision, Funding acquisition, Conceptualization.

Declaration of competing interest

The authors declare that they have no known competing financial interests or personal relationships that could have appeared to influence the work reported in this paper.

Acknowledgement

This research was significantly supported by the COMET project ECHODA (Energy Efficient Cooling and Heating of Domestic Appliances). ECHODA is funded within the framework of COMET – Competence Centers for Excellent Technologies by BMWET, BMIMI, the province of Styria as well as SFG. The COMET program is managed by FFG (application Nr. 50043805 / FFG Nr. 904908). Moreover, the financial support by the Austrian Federal Ministry of Economy, Energy and Tourism, the National Foundation for Research, Technology and Development and the Christian Doppler Research Association is gratefully acknowledged.

Appendix A. Supplementary data

Supplementary data to this article can be found online at https://doi.org/10.1016/j.matdes.2026.115887.

Data availability

Data will be made available on request.

References

[1] M. Ashby, Materials: Engineering, Science, Processing and Design, Elsevier Science & Technology, Oxford, 2007.
[2] C. Levi, J.L. Barton, C. Guillemet, E. Le Bras, P. Lehuede, A remarkably strong natural glassy rod: the anchoring spicule of the Monorhaphis sponge, J. Mater. Sci. Lett. 8 (1989) 337–339, https://doi.org/10.1007/BF00725516.
[3] P. Fratzl, R. Weinkamer, Nature's hierarchical materials, Prog. Mater Sci. 52 (2007) 1263–1334, https://doi.org/10.1016/j.pmatsci.2007.06.001.
[4] J. Aizenberg, J.C. Weaver, M.S. Thanawala, V.C. Sundar, D.E. Morse, P. Fratzl, Skeleton of Euplectella sp.: structural hierarchy from the nanoscale to the macroscale, Science 309 (2005) 275–278, https://doi.org/10.1126/science.1112255.
[5] L. Schretter, D. Şopu, A. Lassnig, J. Eckert, C. Gammer, Enhanced ductility by stress confinement in multilayered glassy thin films, Mater. Des. 259 (2025) 114891, https://doi.org/10.1016/j.matdes.2025.114891.
[6] O. Kolednik, J. Predan, F.D. Fischer, P. Fratzl, Bioinspired Design Criteria for Damage-Resistant Materials with periodically Varying Microstructure, Adv. Funct. Mater. 21 (2011) 3634–3641, https://doi.org/10.1002/adfm.201100443.
[7] P. Fratzl, H.S. Gupta, F.D. Fischer, O. Kolednik, Hindered Crack Propagation in Materials with periodically Varying Young's Modulus—Lessons from Biological Materials, Adv. Mater. 19 (2007) 2657–2661, https://doi.org/10.1002/adma.200602394.
[8] M. Sistaninia, O. Kolednik, Improving strength and toughness of materials by utilizing spatial variations of the yield stress, Acta Mater. 122 (2017) 207–219, https://doi.org/10.1016/j.actamat.2016.09.044.
[9] J. Wiener, F. Arbeiter, O. Kolednik, G. Pinter, Influence of layer architecture on fracture toughness and specimen stiffness in polymer multilayer composites, Mater. Des. 219 (2022) 110828, https://doi.org/10.1016/j.matdes.2022.110828.
[10] J. Stögerer, S. Baumgartner, A. Hochwallner, J. Stampfl, Bio-inspired Toughening of Composites in 3D-printing, Materials (basel) 13 (2020), https://doi.org/10.3390/ma13214714.
[11] D. Madhav, B. Buffel, P. Moldenaers, F. Desplentere, V. Vandeginste, A review of nacre-inspired materials: Chemistry, strengthening-deformation mechanism, synthesis, and applications, Prog. Mater Sci. 139 (2023) 101168, https://doi.org/10.1016/j.pmatsci.2023.101168.
[12] M. Schwaiger, C. Waly, M. Huszar, G. Oreski, M. Feuchter, F. Arbeiter, K. Resch-Fauster, Bioinspired fracture toughness enhancement of a fully bio-based epoxy resin, Polym. Test. 124 (2023) 108098, https://doi.org/10.1016/j.polymertesting.2023.108098.
[13] J. Wiener, F. Arbeiter, A. Tiwari, O. Kolednik, G. Pinter, Bioinspired toughness improvement through soft interlayers in mineral reinforced polypropylene, Mech. Mater. 140 (2020) 103243, https://doi.org/10.1016/j.mechmat.2019.103243.
[14] Y. Estrin, Architectured Materials in Nature and Engineering: Archimats, Springer International Publishing AG, Cham, 2019.
[15] Y. Estrin, Y. Beygelzimer, R. Kulagin, P. Gumbsch, P. Fratzl, Y. Zhu, H. Hahn, Architecturing materials at mesoscale: some current trends, Materials Research Letters 9 (2021) 399–421, https://doi.org/10.1080/21663831.2021.1961908.
[16] M.K. Islam, P.J. Hazell, J.P. Escobedo, H. Wang, Biomimetic armour design strategies for additive manufacturing: a review, Mater. Des. 205 (2021) 109730, https://doi.org/10.1016/j.matdes.2021.109730.
[17] M.Y. Khalid, Z.U. Arif, A. Tariq, M. Hossain, R. Umer, M. Bodaghi, 3D printing of active mechanical metamaterials: a critical review, Mater. Des. 246 (2024) 113305, https://doi.org/10.1016/j.matdes.2024.113305.
[18] M. Bodaghi, A.R. Damanpack, W.H. Liao, Adaptive metamaterials by functionally graded 4D printing, Mater. Des. 135 (2017) 26–36, https://doi.org/10.1016/j.matdes.2017.08.069.
[19] M. Kucewicz, P. Baranowski, J. Małachowski, A. Popławski, P. Płatek, Modelling, and characterization of 3D printed cellular structures, Mater. Des. 142 (2018) 177–189, https://doi.org/10.1016/j.matdes.2018.01.028.
[20] A. Nazir, O. Gokcekaya, K. Md Masum Billah, O. Ertugrul, J. Jiang, J. Sun, S. Hussain, Multi-material additive manufacturing: a systematic review of design, properties, applications, challenges, and 3D printing of materials and cellular metamaterials, Materials & Design 226 (2023) 111661, https://doi.org/10.1016/j.matdes.2023.111661.
[21] N.K. Brown, B. Young, B. Clark, O. Bolmin, B.L. Boyce, P.J. Noell, Optimized design of interlocking metasurfaces, Mater. Des. 233 (2023) 112272, https://doi.org/10.1016/j.matdes.2023.112272.
[22] D. Da, X. Qian, Fracture resistance design through biomimicry and topology optimization, Extreme Mech. Lett. 40 (2020) 100890, https://doi.org/10.1016/j.eml.2020.100890.
[23] D. Da, J. Yvonnet, Topology Optimization for Maximizing the Fracture Resistance of Periodic Quasi-Brittle Composites Structures, Materials 13 (2020) 3279, https://doi.org/10.3390/ma13153279.

[24] Y. Beygelzimer, R. Kulagin, P. Fratzl, Y. Estrin, The Earth's Lithosphere Inspires Materials Design, Adv. Mater. 33 (2021) e2005473, https://doi.org/10.1002/adma.202005473.
[25] M.A. Meyers, P.-Y. Chen, A.-Y.-M. Lin, Y. Seki, Biological materials: Structure and mechanical properties, Prog. Mater Sci. 53 (2008) 1–206, https://doi.org/10.1016/j.pmatsci.2007.05.002.
[26] B.E. Hobbs, A. Ord, Structural geology: the mechanics of deforming metamorphic rocks, Elsevier, Waltham, MA, 2015.
[27] C. Waly, R. Höller, T. Griesser, F. Arbeiter, Deformation and fracture of lithosphere-inspired polymeric multi-layer composites, Results Eng. 24 (2024) 103519, https://doi.org/10.1016/j.rineng.2024.103519.
[28] A. Hohenwarter, Microstructure, strength and fracture toughness of CuNb nanocomposites processed with high pressure torsion using multi-sector disks, Scr. Mater. 189 (2020) 48–52, https://doi.org/10.1016/j.scriptamat.2020.07.061.
[29] R. Kulagin, Y. Beygelzimer, Y. Ivanisenko, A. Mazilkin, B. Straumal, H. Hahn, Instabilities of interfaces between dissimilar metals induced by high pressure torsion, Mater. Lett. 222 (2018) 172–175, https://doi.org/10.1016/j.matlet.2018.03.200.
[30] X.Y. Chan, Z.H. Ng, L. Guan, H. He, S. Sapasakulvanit, P. Dee, H. Le Ferrand, Fabrication and Testing of Bioinspired Composites with Curved Multilayer Microstructures, JOM 75 (2023) 2158–2173, https://doi.org/10.1007/s11837-023-05705-w.
[31] R. Bermejo, "Toward seashells under stress": Bioinspired concepts to design tough layered ceramic composites, J. Eur. Ceram. Soc. 37 (2017) 3823–3839, https://doi.org/10.1016/j.jeurceramsoc.2017.04.041.
[32] A. Tiwari, J. Wiener, F. Arbeiter, G. Pinter, O. Kolednik, Application of the material inhomogeneity effect for the improvement of fracture toughness of a brittle polymer, Eng. Fract. Mech. 224 (2020) 106776, https://doi.org/10.1016/j.engfracmech.2019.106776.
[33] E. Martin, B. Poitou, D. Leguillon, J.M. Gatt, Competition between deflection and penetration at an interface in the vicinity of a main crack, Int. J. Fract. 151 (2008) 247–268, https://doi.org/10.1007/s10704-008-9228-0.
[34] M. Pletz, F.J. Arbeiter, Combined Crack Initiation and Crack Growth Model for Multi-Layer Polymer Materials, Materials (basel) 15 (2022), https://doi.org/10.3390/ma15093273.
[35] D. Leguillon, Strength or toughness? A Criterion for Crack Onset at a Notch, European Journal of Mechanics - A/solids 21 (2002) 61–72, https://doi.org/10.1016/S0997-7538(01)01184-6.
[36] D. Taylor, The theory of critical distances, Eng. Fract. Mech. 75 (2008) 1696–1705, https://doi.org/10.1016/j.engfracmech.2007.04.007.
[37] M. Pletz, S.M. Frankl, C. Schuecker, Evaluation of existing and introduction of new incremental crack propagation approaches in FEM, Theor. Appl. Fract. Mech. 131 (2024) 104452, https://doi.org/10.1016/j.tafmec.2024.104452.
[38] S.M. Frankl, M. Pletz, C. Schuecker, Improved concept for iterative crack propagation using configurational forces for targeted angle correction, Eng. Fract. Mech. 266 (2022) 108403, https://doi.org/10.1016/j.engfracmech.2022.108403.
[39] R. Mueller, G.A. Maugin, On material forces and finite element discretizations, Comput. Mech. 29 (2002) 52–60, https://doi.org/10.1007/s00466-002-0322-2.
[40] M. Cervera, G.B. Barbat, M. Chiumenti, J.-Y. Wu, A Comparative Review of XFEM, Mixed FEM and Phase-Field Models for Quasi-Brittle Cracking, Arch Computat Methods Eng 29 (2022) 1009–1083, https://doi.org/10.1007/s11831-021-09604-8.
[41] G. Molnár, A. Doitrand, R. Estevez, A. Gravouil, Toughness or strength? Regularization in Phase-Field Fracture Explained by the Coupled Criterion, Theoretical and Applied Fracture Mechanics 109 (2020) 102736 https://doi.org/10.1016/j.tafmec.2020.102736.
[42] S.T. Nabavi, H. Fossen, Fold geometry and folding – a review, Earth Sci. Rev. 222 (2021) 103812, https://doi.org/10.1016/j.earscirev.2021.103812.
[43] D20 Committee, Test Methods for Plane-Strain Fracture Toughness and Strain Energy Release Rate of Plastic Materials, ASTM International, West Conshohocken, PA.
[44] ISO 13586:2018, Plastics — Determination of fracture toughness (GIC and KIC) — Linear elastic fracture mechanics (LEFM) approach, International Organization for Standardization (ISO) 83.080.01, 2018. https://www.iso.org/standard/67721.html.
[45] L. Zorzetto, L. Andena, F. Briatico-Vangosa, L. de Noni, J.-M. Thomassin, C. Jérôme, Q. Grossman, A. Mertens, R. Weinkamer, M. Rink, D. Ruffoni, Properties and role of interfaces in multimaterial 3D printed composites, Sci. Rep. 10 (2020) 22285, https://doi.org/10.1038/s41598-020-79230-0.
[46] V. Slesarenko, S. Rudykh, Towards mechanical characterization of soft digital materials for multimaterial 3D-printing, Int. J. Eng. Sci. 123 (2018) 62–72, https://doi.org/10.1016/j.ijengsci.2017.11.011.
[47] L. Wang, J. Lau, E.L. Thomas, M.C. Boyce, Co-continuous composite materials for stiffness, strength, and energy dissipation, Adv. Mater. 23 (2011) 1524–1529, https://doi.org/10.1002/adma.201003956.
[48] X. Mi, N. Liang, H. Xu, J. Wu, Y. Jiang, B. Nie, D. Zhang, Toughness and its mechanisms in epoxy resins, Prog. Mater Sci. 130 (2022) 100977, https://doi.org/10.1016/j.pmatsci.2022.100977.
[49] Y. Li, Z. Teng, Effect of printing orientation on mechanical properties of SLA 3D-printed photopolymer, Fatigue Fract Eng Mat Struct 47 (2024) 1531–1545, https://doi.org/10.1111/ffe.14265.
[50] S. Lu, A. Laborda, R. Cook, Y. Zhang, R. Verbickas, P. Reed, A numerical study of crack shielding/anti-shielding in layered architectures, Int. J. Fatigue 124 (2019) 503–519, https://doi.org/10.1016/j.ijfatigue.2019.03.030.
[51] Masoud Sistaninia, Application of the configurational forces concept for the design of tough, strong and damage-tolerant composites (2017).
[52] S. Mengsha, Z. Chunyu, C. Yuheng, W. Biao, Experimental and theoretical evaluation of influence of hole size on deformation and fracture of elastic perforated plate, Mech. Mater. 187 (2023) 104841, https://doi.org/10.1016/j.mechmat.2023.104841.
[53] Stress Concentration at Notches, in: Fatigue of Structures and Materials, secondnd ed., Springer, [Berlin], [Heidelberg], op, 2010, pp. 59–88.
[54] J. Kechagias, S. Zaoutsos, Effects of 3D-printing processing parameters on FFF parts' porosity: outlook and trends, Mater. Manuf. Process. 39 (2024) 804–814, https://doi.org/10.1080/10426914.2024.2304843.
[55] G.W. Ehrenstein, Polymer Werkstoffe: Struktur Eigenschaften Anwendung, third. Auflage, Hanser Verlag, München, 2011.
[56] F. Richter, D. Wu, Interfacial adhesion between dissimilar thermoplastics fabricated via material extrusion-based multi-material additive manufacturing, Mater. Des. 252 (2025) 113688, https://doi.org/10.1016/j.matdes.2025.113688.
[57] C. Waly, V.D. Pires, P. Beier, S. Schulnig, I. Duretek, M. Pletz, F. Arbeiter, Towards predicting failure modes in multi-material extrusion-based additive manufactured PETG/TPC structures, Theor. Appl. Fract. Mech. 141 (2026) 105251, https://doi.org/10.1016/j.tafmec.2025.105251.